

Streamline-based method for intra-day solar forecasting through remote sensing

Lukas Nonnenmacher, Carlos F.M. Coimbra*

Department of Mechanical and Aerospace Engineering, Jacobs School of Engineering, Center for Renewable Resource Integration and Center for Energy Research, University of California, 9500 Gilman Drive, La Jolla, CA 92093, USA

Received 25 March 2014; received in revised form 30 July 2014; accepted 31 July 2014
Available online 24 August 2014

Communicated by: Associate Editor Frank Vignola

Abstract

This work presents an enhanced deterministic solar irradiance forecasting approach that relies on satellite images and ground measurements as inputs. The proposed method is based on a ground-truth improved satellite-to-irradiance model for the prediction of global horizontal irradiance (*GHI*). This approach relies on cloud tracking and advection with an optical flow algorithm. The application of the optical flow algorithm between two consecutive satellite image frames allows for the calculation of a vector field covering each pixel in the satellite image. This cloud motion vector (*CMV*) field determines the streamline passing through the location of interest. The estimated cloud advection along the quasi-steady streamline to the location of interest is then computed, and this information is translated into an irradiance forecast for the location of interest. In order to reduce the error associated with a linear satellite-to-irradiance model, a novel approach employing ground measurements is proposed. Additionally, decision heuristics are identified and implemented to issue a forecast based on *CMV* or persistence, depending on the current sky conditions. The overall method is tested for over 110 days of operational 1-, 2- and 3-h ahead *GHI* forecasts, implemented and evaluated for San Diego, California. The continual forecasting skill of this method for the 110 days ranges between 8% and 19% over persistence, depending on the forecast horizon. While previously proposed methods achieve similar skills, the completely deterministic approach combined with comparably low computation and implementation costs makes the proposed method suitable for applications with limited availability of data.

© 2014 Elsevier Ltd. All rights reserved.

Keywords: Solar forecasting; Remote sensing; Cloud tracking; Optical flow; Global horizontal irradiance

1. Introduction

Solar power is a virtually inexhaustible energy resource that is likely to play an increasing role in the future energy supply of most, if not all, societies. While technological improvements enable more efficient and cost effective solar power generation, the fluctuation of solar irradiance at the surface of the Earth still constitutes a major obstacle for power grid integration. Solar forecasting on multiple time

horizons is an effective approach to mitigate the adverse effects of variable solar power generation on the operation and management of the electric grid. A detailed review of current solar forecasting methods can be found in [Inman et al. \(2013\)](#). While short term forecasts (intra-hour) became more sophisticated based on recent advances in ground based sky-imagery and modeling techniques ([Chow et al., 2011](#); [Ghonima et al., 2012](#); [Marquez and Coimbra, 2013a](#); [Dong et al., 2013](#); [Handa et al., 2014](#)), intra-day methods still lack accuracy. Several previous studies propose and evaluate methods for intra-day forecasts ([Mathiesen and Kleissl, 2011](#); [Marquez et al., 2013](#)).

* Corresponding author.

E-mail address: cocoimbra@ucsd.edu (C.F.M. Coimbra).

Nomenclature

<i>ANN</i>	artificial neural network	<i>PIV</i>	Particle Image Velocimetry
<i>CDF</i>	cumulative distribution function	<i>RMSE</i>	root mean squared error
<i>CMV</i>	cloud motion vector	<i>RTM</i>	radiative transfer model
<i>CS</i>	clear sky	<i>T</i>	threshold
<i>DCA</i>	Difference Centroid Algorithm	<i>UTC</i>	Coordinated Universal Time
<i>DNI</i>	direct normal irradiance	\vec{V}	average velocity vector of streamline
<i>Err.</i>	Error calculated as $Err. = \Delta GHI = GHI_{GT} - GHI_F$	<i>X</i>	probability bin
$GHI_{CS,GT}$	global horizontal irradiance, indices: CS – clear sky, GT – ground truth	<i>a</i>	shift parameter
$GHI_{M1,M2}$	global horizontal irradiance, M1, M2 – irradiance Models 1 and 2	<i>i, j</i>	summation indices
GHI_{kt}	global horizontal irradiance modeled with k_t -persistence	k_t	clear-sky index
\widehat{GHI}, GHI_F	global horizontal irradiance forecasted with the proposed method	<i>k, l</i>	geometric averaging parameters
<i>GOES</i>	Geostationary Operational Environmental Satellite	<i>n</i>	linear cloud index
$I(x, y, t)$	brightness of pixel at location <i>x, y</i> at time <i>t</i>	<i>p, q</i>	number of pixels in the <i>x</i> - & <i>y</i> -direction
<i>Im</i>	downloaded satellite image	<i>px</i>	pixel
<i>L</i>	geometrical length	<i>s</i>	forecasting skill
<i>MAE</i>	mean absolute error	<i>u</i>	velocity in <i>x</i> -direction (horizontal)
<i>MBE</i>	mean bias error	<i>v</i>	velocity in <i>y</i> -direction (vertical)
<i>MFR-7</i>	multi filter radiometer	<i>xcor</i>	cross correlation
<i>N</i>	number of bins	$\bar{\alpha}$	average albedo image
<i>NOAA</i>	National Oceanic and Atmospheric Administration	β	cloud fraction image
<i>NWP</i>	numerical weather prediction	Δt	forecast horizon
		δ, ϵ	penalty function parameters
		$\vec{\zeta}$	streamline vector
		η	cloud index image
		λ	regularization parameter
		ρ	pixel intensity, max & min occurring in data set
		$Q_{S,D}$	spatial and data penalty functions

However, especially the direct use of satellite images is currently not very common due to difficulties concerning data availability, albedo correction, resolution, cloud segmentation and tracking and real time processing of images. Previous methodologies utilizing satellite images for solar forecasting have been proposed by [Hammer et al. \(1999, 2003\)](#) and [Marquez et al. \(2013\)](#). This contribution seeks to take advantage of the online near real-time availability of processed satellite images derived from the visible channel (0.55–0.75 μm) of the Geostationary Operational Environmental Satellites West and East (*GOES-W* and *GOES-E*) with a resolution of approximately 1 km, combined with a fast cloud segmentation algorithm. Two consecutive frames of cloud index images (η s) are the foundation for the application of an advanced optical flow algorithm proposed by [Sun et al. \(2010\)](#), applied to derive cloud motion vectors (*CMV*) between two consecutive frames. This approach also enables the derivation of cloud velocity. Optical flow was found the most suitable approach for cloud tracking during this study, while other cloud tracking methods were the topic of several previous publications ([Endlich and Wolf, 1981](#); [Guillot et al., 2012](#); [Escrig et al., 2013](#)). The *CMV* field and velocities

are utilized to calculate the streamline of the flow field reaching the location of interest. This streamline enables the identification of an area of pixels most likely to propel to the location of interest. All of these inputs are deterministic and therefore provide a method that can be applied without any training for every location covered by satellite images. This method is heavily based on the performance of a satellite-to-irradiance model that translates the identified region of cloud intensity values into forecast values of *GHI* at the region of interest. In this context, a ground measurement enhanced semi-empirical satellite-to-irradiance model has been developed.

This work is divided into two main parts, the satellite-to-irradiance model and the forecasting model. Section 2 gives an overview of previously proposed methods covering the same forecast horizons for *GHI* and highlights the purpose for this study. Section 3 focuses on the processing of the satellite images provided by National Oceanic and Atmospheric Administration (*NOAA*), the applied cloud segmentation and the satellite-to-irradiance model. Section 4 includes the selection of a cloud tracking method, cloud tracking with optical flow and the deterministic solar irradiance forecasting approach. Section 5 contains the

evaluation metrics for the satellite-to-irradiance model and for the forecasts. Results of the overall methodology for the location of San Diego, California are discussed. Section 6 includes conclusions, prospective applications and open research questions based on the results.

2. Background

The field of solar irradiance and photovoltaic power output prediction increased rapidly within the last decade. Various previous studies covered (multiple) hour ahead *GHI* forecasts, based on several different methods. In general it can be distinguished between statistical, machine learning, image based and numerical weather prediction (NWP) based methods. Satellite image based forecasts are among the most promising approaches for 1–3h ahead forecasts. An early approach in satellite based solar irradiance forecasting was proposed by Hammer et al. (1999) where clouds are segmented from images captured by the Meteosat satellite and tracked based on a statistical algorithm. The cloud motion is then extrapolated and prospectively advected cloud regions are translated into the forecast by the satellite-to-irradiance model. Lorenz et al. (2007) showed that the forecasting accuracy based on satellite images outperforms NWP based predictions for forecast horizons up to 4h ahead. Perez et al. (2010) followed this general approach and applied it for images from the GOES satellites. Based on an evaluation covering seven locations, Perez et al. (2010) found that the satellite based model outperforms NWP derived forecasts for up to 5 h ahead. Marquez et al. (2013) combined the CMV based approach with artificial neural networks (ANNs) to create a hybridized forecast. The performance of the hybrid approach is at par or improves previously obtained results.

Motivated by the results presented in Hammer et al. (1999), Lorenz et al. (2007) and Perez et al. (2010), this study proposes an advanced implementation of the previously proposed deterministic satellite-based forecasting techniques with various crucial refinements that are necessary to achieve good forecast performance in a highly variable and difficult to predict solar micro-climate. An unrefined application of deterministic, linear cloud advection based on precise cloud tracking and without the decision heuristics leads to a negative forecasting skill for the test location in San Diego. This is partially due to the impact of frequently forming inversion layers over the Pacific Ocean.

3. Data processing and satellite-to-irradiance model

Fig. 1 summarizes the data flow in the present work, including the derivation of cloud index images (η) from satellite images pre-processed by NOAA. The cloud index images are used for the satellite-to-irradiance model and the forecast model. The forecast model includes cloud tracking based on optical flow to derive the cloud motion vectors (CMVs). The CMVs are used for streamline and

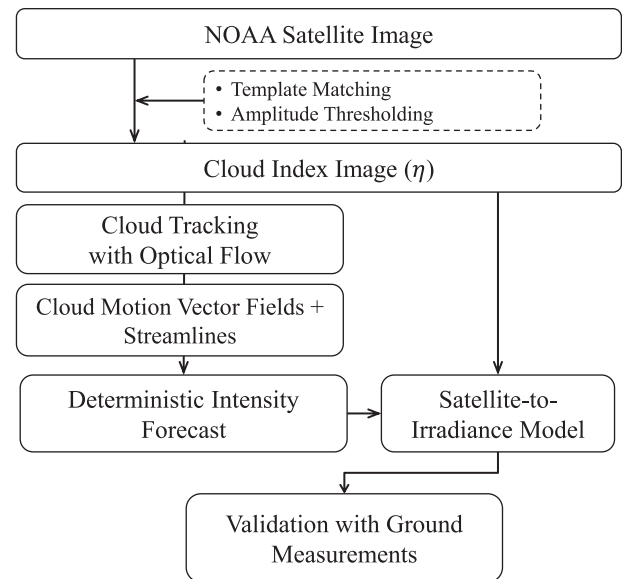


Fig. 1. Schematic of data processing for the satellite-to-irradiance model based solar forecasting system.

velocity calculations. Both are utilized to identify advecting cloud regions. The last step consists of the validation of the methodology by means of ground telemetry.

3.1. Ground based irradiance measurements

Ground measurements have been obtained at a solar observatory equipped with a multi-filter radiometer (MFR-7) by the make Yankee Environmental Systems in San Diego, California. A detailed description of the deployed solar observatory and the climate characteristics at the locations are available in Nonnenmacher et al. (2014). This data is considered to represent the ground truth. Data sets were collected on a 1 min sample rate and averaged to provide 15 min values.

3.2. Satellite images

Relevant satellite images are accessed via NOAA every 15 min during daylight times with an automated download script. The time interval of 15 min is chosen since the ground truth validation location (San Diego, California) lies in a narrow band where the recorded areas of the GOES-West and GOES-East satellites overlap. Therefore, images are usually available every 15 min. The most recent satellite images are available online at <http://sat.wrh.noaa.gov/satellite/1km/sandiego/vis1san.gif>. The period of study ranged from March 2013 to March 2014. The images are pre-processed by NOAA. This enables a clear distinction between clouds and Earth surface without additional correction for the changing sun elevation angle during the diurnal cycle. The images are downloaded as Portable Network Graphics including a superimposed land mask. The land mask lines are replaced by not-a-number values based on their color. These images are used to derive cloud

segmented images, also called cloud indexed images (η s). Cloud segmentation to derive η s is important for two purposes: (1) irradiance modeling at the Earth surface, and (2) computationally optimized cloud motion detection and cloud speed calculations. This step is crucial for the application of a satellite-to-irradiance model and the difference centroid algorithm based cloud tracking. It additionally reduces computation costs for cloud tracking based on optical flow. The location of the ground based solar observatory in the satellite image has been identified with triangulation based on distinct geographical features. This estimation has been optimized and verified by applying the satellite-to-irradiance model described below for all pixels in a 30 by 30 pixel area by identifying the one with the best correlation to the ground data. The downloaded satellite image is cut to a domain size of 200 by 200 pixels with the location of interest in the center to reduce computation costs. This domain size was chosen empirically based on the observation that it is very unlikely that clouds from outside of this domain are propelled to the location of interest within the studied time horizons.

3.3. Cloud segmentation

While the general idea of cloud tracking goes back to the first imagery from satellites, cloud extraction by image segmentation as part of an automated weather forecasting system was introduced much later by [Leung and Jordan \(1995\)](#). To be able to translate a *NOAA* satellite images into η , only the following two steps out of the originally 6 steps mentioned by [Leung and Jordan \(1995\)](#) are necessary:

- (1) *Template matching* to identify pixels showing the ground with its region specific albedo. The template has been generated from about 150 manually selected images from clear days. The average albedo image can then be calculated with the equation:

$$\bar{\alpha} = \frac{1}{N} \sum_{i=1}^N Im_{clear}, \quad (1)$$

where $\bar{\alpha}$ indicates the derived average ground albedo map and Im_{clear} stands for the manually selected satellite images with no clouds (clear images). If certain regions over the Pacific Ocean have not been free of clouds, the cloud covered areas have been replaced with values of cloudless regions over the ocean. A well known problem in irradiance modeling based on satellite images is caused by areas with snow cover due to irradiance reflectivity similar to clouds. While this is a problem in certain areas and interferes with cloud detection, the error introduced by this effect is neglected since the areas of occurrence are not in proximity to the areas of interest of this study.

- (2) *Amplitude thresholding* to separate clouds from ground pixels. To filter the noise introduced by the mismatch of the average ground albedo template to the background, the threshold filter can be set empirically:

$$\eta_{x,y} = \begin{cases} \eta_{x,y} = 0 & \text{if } |(Im_{x,y} - \bar{\alpha}_{x,y})| \leq T, \\ \eta_{x,y} = Im_{x,y} & \text{if } |(Im_{x,y} - \bar{\alpha}_{x,y})| > T, \end{cases} \quad (2)$$

where η represents the derived cloud indexed image, Im stands for the latest available satellite image pre-processed by *NOAA* and T is the applied threshold filter. For this study, $T = 3$ has been chosen. As mentioned above, $\bar{\alpha}_{x,y}$ indicates pixel intensity values from the average albedo image at the x - and y -location.

[Fig. 2](#) shows $\bar{\alpha}$, calculated according to Eq. (1), Im as downloaded from the *NOAA* website and the derived η , calculated with Eq. (2) as an example for 13-June-2013 20:45 Coordinated Universal Time (*UTC*). It can be seen that the cloud separation works well in most regions. However, difficulties exist due to the threshold filter in areas where thin clouds are present (e.g. in the north east area of the example shown in [Fig. 2](#)). Since the threshold filter only affects very thin clouds and the *GHI* attenuation by thin clouds is limited, the error introduced by this procedure can be neglected. Additionally to the η s, a binary cloud fraction image (β) is calculated as follows:

$$\beta_{x,y} = \begin{cases} \beta_{x,y} = 0 & \text{if } \eta_{x,y} = 0, \\ \beta_{x,y} = 1 & \text{if } \eta_{x,y} > 0, \end{cases} \quad (3)$$

This β is important for the decision heuristics listed under [Section 4.6](#).

3.4. Satellite-to-irradiance model

3.4.1. Linear model (Model 1)

A common approach for a satellite-to-irradiance model is to relate the pixel intensity values to irradiance conditions (e.g. [Cano et al., 1986](#); [Pereira et al., 2000](#); [Schillings et al., 2004](#); [Perez et al., 2002](#)). This is also utilized in previous studies covering satellite based solar irradiance forecasting models (e.g. [Hammer et al., 1999](#); [Marquez et al., 2013](#)). While most of the satellite-to-irradiance models are based on unprocessed satellite images, a big part of the image processing to derive η in those cases is dedicated to correct for the changing albedo with varying sun elevation angle. Since the images used in this study already appear to be corrected for changing albedo, this traditional approach can be easily applied to the η s here. The traditional approach, as proposed by [Cano et al. \(1986\)](#), models the irradiance based on the η by utilizing the concept of the linear cloud index as follows:

$$n = \frac{\rho - \rho_{min}}{\rho_{max} - \rho_{min}}, \quad (4)$$

where n presents the linear cloud index, ρ refers to the reflectance scanned by the satellite at an instant (also called instantaneous planetary albedo or intensity) while ρ_{max} and ρ_{min} refer to the maximum and minimum occurring

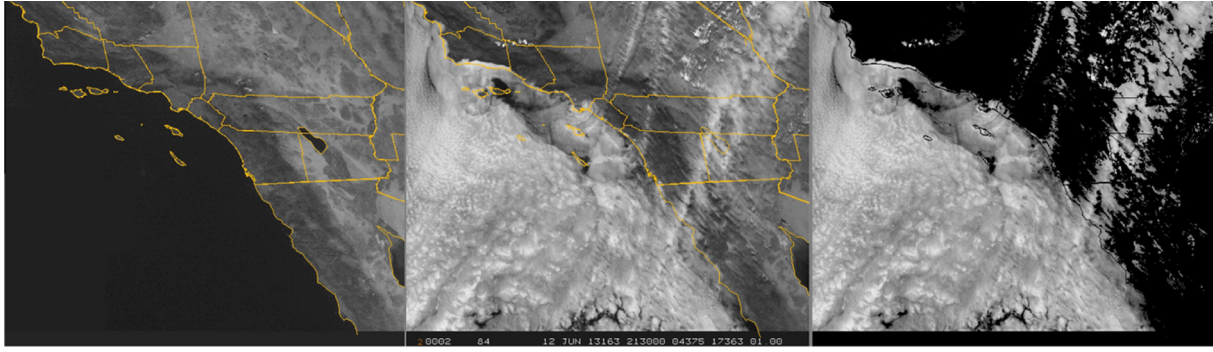


Fig. 2. Example of the applied image processing steps to derive the cloud index image (η) for 13-June-2013. The left image shows the average ground albedo image ($\bar{\alpha}$) derived by averaging 150 satellite images with clear conditions. This image is used as the ground albedo template. The middle image shows the used *NOAA* satellite image (Im) as downloaded from the *NOAA* website. The right image shows the η derived by removing areas that match the albedo template shown in the left image. A threshold filter is applied to take variations from the average image into account. In general, this approach works well for optically thick clouds. Thin clouds are challenging to detect due to the threshold filter. This effect can be seen by comparing the middle and the right image especially in the north east area. In these areas there are also difficulties in distinguishing between ground and clouds with the unaided eye.

intensity value in a large image data base. The GHI can then be modeled by applying the following equation:

$$GHI_{M1} = GHI_{CS} \cdot (1 - n), \quad (5)$$

where GHI_{CS} represents the expected GHI values under clear sky conditions as calculated with the model developed by Ineichen (2006), Ineichen and Perez (2002) and Gueymard (2012). This approach relies on a linear relationship and is frequently used for several applications (e.g. Heliosat method, for details please see Beyer et al., 1996). Multiple approaches have been taken to improve the linear model to achieve higher accuracy (Girodo et al., 2006; Martins et al., 2007; Mueller et al., 2004). The statistical results of the validation of the linear model with ground measurements are discussed in Section 5.2. To optimize the accuracy for the utilized *NOAA* satellite images, Model 2 was created.

3.4.2. Statistical model (Model 2)

The model described above is popular and commonly applied to model solar irradiance if only satellite images are available. Nevertheless, the performance of this approach can be enhanced significantly with ground measurements. A high performance of the satellite-to-irradiance model is of crucial importance for a deterministic satellite image based irradiance forecast since the error in the satellite-to-irradiance model propagates into the error of the forecast. Since ground measurements are available for this study, statistical values over longer periods can be calculated and utilized. Mueller et al. (2009) proposed the usage of a lookup table for a satellite-to-irradiance model for optimized accuracy and calculation costs. We pick up this approach and relate an intensity value ρ to the statistical mean of k_t calculated by:

$$k_{t,M2}(\rho) = \frac{\overline{GHI}_{GT}(\rho)}{GHI_{CS}} = (1 - n_{M2}), \quad (6)$$

where ρ is the intensity value from η ranging between 24 and 44 but including 0 which indicates clear sky conditions. $\overline{GHI}_{GT}(\rho)$ is the average measured GHI value occurring for

ρ and GHI_{CS} is the clear sky value calculated with a clear sky model mentioned above. Therefore, the lookup table contains 22 elements (see Table 1). GHI is modeled by:

$$GHI_{M2} = GHI_{CS} \cdot k_{t,M2}(\rho), \quad (7)$$

where $k_{t,M2}$ is used as assigned by the created lookup table and GHI_{CS} is the clear sky value. The lookup table used for this study has been created with 4700 satellite image frames and corresponding ground measurements for the location in San Diego. Results of the two satellite-to-irradiance models are discussed and compared in Section 5.2.

SolarAnywhere[®] provides irradiance time series covering the continental US and Hawaii based on the SUNY model v2.0 (as proposed by Perez et al. (2002)). To have a reference to compare the accuracy of the two models shown here, results from the SUNY model from the same period of the previous year (due to data availability) have been added to Table 2. The SUNY model has been extensively studied and validated (e.g. Vignola et al., 2007; Nottrott and Kleissl, 2010; Gueymard and Wilcox, 2011; Djebbar et al., 2012). SUNY data was accessed via SolarAnywhere[®] with a temporal resolution of 30 min.

Table 1

Lookup table for the satellite-to-irradiance model created from mean k_t values based on ground measurements in San Diego. While these k_t values are optimized for San Diego, they presumably also provide an improvement over Model 1 for other locations (validated for Davis, California).

Intensity value ρ	k_t	Intensity value ρ	k_t
0	1.00000	34	0.36192
24	0.65228	35	0.33400
25	0.61249	36	0.28652
26	0.58331	37	0.25848
27	0.56444	38	0.27137
28	0.53644	39	0.23905
29	0.52786	40	0.22012
30	0.48311	41	0.20566
31	0.47338	42	0.16433
32	0.41145	43	0.16804
33	0.34690	44	0.17806

Table 2

Comparison between results from the satellite-to-irradiance models used in this study and available data from the SolarAnywhere® data set. Note that the modeled data was derived for 2013 whereas the SUNY data was for 2012 due to availability. However, the mismatch of years does not interfere with the purpose to show the usability of the described and implemented satellite-to-irradiance model. Since the lookup table approach outperforms the other method, it is used for the proposed forecasting method.

San Diego	Mean measured (W m ⁻²)	Mean modeled (W m ⁻²)	MBE (W m ⁻²)	rMBE (%)	MAE (W m ⁻²)	rMAE (%)	RMSE (W m ⁻²)	rRMSE (%)	xcor (–)
NOAA GHI Model 1	493.49	495.73	–2.25	–0.46	71.72	14.53	124.53	25.24	0.934
NOAA GHI Model 2	493.49	516.78	–23.29	–4.72	61.72	12.51	107.41	21.77	0.95
SUNY GHI	385.31	455.16	–69.86	–18.13	106.40	27.61	213.14	55.32	0.825
SUNY GHI (outliers removed)	415.95	439.89	–23.95	–5.76	64.71	15.56	130.52	31.38	0.932

4. Cloud tracking and forecasting method

4.1. Cloud tracking testbed

Cloud tracking is often used for velocity field calculations for both, ground and satellite based imagery. The general approach for CMV field calculations is always based on the calculation of displacement of image features between two image frames. However, the features that are tracked as well as the optimization approach to identify the same feature in two similar but not identical images can be quite different. While various feature tracking algorithms exist, three have been pre-selected for an initial feasibility test on an artificial cloud tracking test bed. For pre-selection, a detailed description about the implementation of the algorithm had to be available and the algorithms had to be suitable for a local computer. The three commonly applied methods are: (1) Difference Centroid Algorithm (*DCA*), (2) Particle Image Velocimetry (*PIV*), and (3) Optical Flow. For details about the implementation of these methods see Shi (1998), Marquez et al. (2013) and Sun et al. (2010). Previous satellite based solar irradiance prediction methods calculate CMV fields solely based on statistical approaches as in Hammer et al. (1999) or *PIV* as in Marquez et al. (2013). The CMV fields are the foundation for the calculation of a streamline that is used for forecasting as described below in this section. The feasibility of these algorithms has been tested on a test bed, covering three artificially created cloud movement cases. Case represents the linear movement of a cloud field through consecutive satellite images. Case represents linear movement of two distinct cloud fields in opposite directions. Case resembles linear cloud movement under highly variable conditions with forming and dissolving parts of the cloud field. Multiple artificial η have been created manually by moving and modifying cloud fields with known displacements between two frames. Based on this tracking test bed, the *DCA* does not identify cloud movement in complex conditions. While the *DCA* has an advantage due to its simplicity in implementation, it lacks robustness under broken sky conditions to unambiguously identify the right centroids if the number varies between two frames due to cloud evaporation, condensation, and precipitation (test bed case 3). Therefore, the *DCA* is not suitable for more complex tasks of cloud tracking and is not considered further during this study. The *PIV*

and the optical flow algorithms continuously identify the displacement correctly based on this test bed and therefore perform equally well. However, since the optical flow algorithm is an open source code in contrast to the commercial *PIV* software that has been used, the optical flow algorithm has been applied for the remainder of this study.

4.2. Optical flow algorithm

Several optical flow methods have been developed and optimized in numerous approaches. Their optimization are subject of current research for many computer vision applications. However, little effort has been made to apply these methods to track clouds segmented from satellite images. Collet et al. (1992) and Wu (1995) are the only publication that apply optical flow algorithms for cloud motion tracking known to the authors. A summary of the utilized algorithm as presented in Sun et al. (2010, 2014) is given here. More specific details are given in the references (Horn and Schunck, 1981; Black and Anandan, 1996; Sun et al., 2010). A well documented, free implementation of the optical flow algorithm is provided by Sun et al. (2010) as Matlab functions that have been used throughout this study. The method named *classic++* described by Sun et al. (2010) has been identified as the most suitable approach for the purpose of cloud tracking, especially with regards to accuracy and processing times. The selection was based on a small test set (approximately 10 days worth of satellite images) by the achievement of the highest forecasting skill for those days with the developed method. The optical flow implementation provided by Sun et al. (2010) used for this study is based on the global formulation originally introduced by Horn and Schunck (1981). The first main assumption of brightness constancy is simply that the brightness of an image feature at location (x, y) remains constant while it is displaced between two frames to the position $(x + \Delta x, y + \Delta y)$ (initial implementation of optical flow). This holds true for most situations present in η . However, two simplifications about the cloud fields are implied in this assumption: (1) The cloud field formation, deformation and evaporation is negligible compared to the horizontal displacement, (2) the velocity of the cloud field is constant over the thickness. Intensity is generally referred to as ρ for satellite-to-irradiance models while the same variable is

generally refereed to as brightness (I) in computer vision. To obey conventional nomenclature, we use I for the brightness when referring to optical flow calculations. We can write the following equation:

$$I(x, y, t) = I(x + u\Delta t, y + v\Delta t, t + \Delta t), \quad (8)$$

where I indicates the brightness at the location (x, y) at time t of the η . Δt is the time passing between two consecutively available η s. Intensity values will be referred to as I_1 (first image) and I_2 (consecutive image) from now on. This is the basic equation defining the general approach to the detection of optical flow. For this equation, a set of additional constraints are needed to allow for solution. These additional constraints can be derived via several ways, e.g. correlation methods, gradient methods or regression methods (Black and Anandan, 1996). According to Sun et al. (2010) the spatially discrete classical optical flow objective function can be written as:

$$F(u, v) = \sum_{x,y} \{ \varrho_D(I_1(x, y) - I_2(x + u_{x,y}, y + v_{x,y})) + \lambda [\varrho_S(u_{x,y} - u_{x+1,y}) + \varrho_S(u_{x,y} - u_{x,y+1}) + \varrho_S(v_{x,y} - v_{x+1,y}) + \varrho_S(v_{x,y} - v_{x,y+1})] \}, \quad (9)$$

where F refers to the calculated flow field with the u and v velocities in the x - and y -direction. The variables ϱ_S and ϱ_D refer to the spatial and data penalty functions. The penalty function ϱ combines the data term (subscript D) that assumes constant image properties with the spatial term (subscript S) that models how flow is expected to vary across the image. The combination of these terms is optimized with an objective function. λ is the regularization parameter. Based on the study of Sun et al. (2010), $\lambda = 3$ was used based on the performance on the Middlebury test. As suggested in Bruhn et al. (2005), a Charbonnier penalty function is used as:

$$\varrho(x) = (x^2 + \epsilon^2)^{0.45}, \quad (10)$$

for both, data and spatial penalty in the x -direction (y -direction similarly), ϵ is the variation parameter. Based on the used implementation $\epsilon = 0.001$.

4.3. Streamline and velocity

A key part of the deterministic forecast is based on the calculation of the streamline that passes through San Diego in the CMV field. Streamlines in the 2-dimensional space are calculated by definition as:

$$\frac{dx}{u} = \frac{dy}{v}, \quad (11)$$

where dx and dy are line elements of the streamline of arc length. The local velocity in the x and y direction are indicated by u and v and given by the calculated CMV field. After this application, we obtain a streamline passing through the location of interest as a vector of the form $\vec{\zeta} = (x_1, \dots, x_n, y_1, \dots, y_n)$. It is straight forward to only

use the upstream part of the streamline. After the streamline has been obtained, the average velocity vector for the streamline between two frames can be calculated by:

$$\vec{V} = \frac{1}{N} \sum_{i=1}^N (u_i, v_i) \quad (12)$$

where u and v are indicating the x - and y -velocities of the CMV field covered by the streamline $\vec{\zeta}$ ($i \in \vec{\zeta}$). This leaves us with a speed in vector form derived in the unit pixel per frame ($px/frame$). The magnitude of the velocity can be obtained by taking $|\vec{V}|$ rounded to the next integer. From here on, we know the directions of cloud flow as well as the associated velocity.

4.4. Forecasting model

After the calculation of the streamline and the associated average velocity, a forecast can be issued under the assumption that the identified CMV field between η_t and η_{t+1} will persist and that the velocity \vec{V} can be extrapolated to the time horizon of interest (frozen cloud assumption). Based on these parameters, the conditions likely to propel to the location of interest in the time horizon of interest can be identified (see Fig. 3 for an example). The cloud conditions over this region can be translated to an irradiance forecast based on the satellite-to-irradiance model discussed above. Therefore, the forecast can be issued according to the following:

$$\hat{\rho}_t = \eta(\vec{\zeta}(x_n, y_n)), \quad (13)$$

where x_n and y_n are the vector elements of the streamline that are presumably propelling to the location of the forecast. This leaves us with an intensity value $\hat{\rho}_t$ that can be used for the satellite to irradiance model. To identify the pixel on the streamline that is likely to be propelled to the location of interest, we have to define the shift parameter $a = 1 + |v| \cdot \Delta t$. In this study, predicted values will be superimposed with a $\hat{\cdot}$ -symbol, e.g. \widehat{GHI} . Since the previously mentioned assumptions are a simplification for a significantly more complex system, the forecasting skill can be enhanced by taking surrounding pixels into account. The basic function for a spatial averaging filter for a region of $p \times q$ pixels is given by Nakariyakul (2013) as:

$$g(x, y) = \frac{1}{p \cdot q} \sum_k \sum_l f(x - k, y - l) \quad (14)$$

where $f(x, y)$ is the input region and $g(x, y)$ is the averaged output region, while k and l represent the size of the averaging window in the x - and y -direction, respectively. The averaging area was chosen to be square ($k = l$) and was optimized with the development set. It has been found to be $k = 8$ pixels for the 1h-ahead forecast, $k = 10$ pixels for the 2h ahead forecast and $k = 11$ pixels for the 3h ahead forecast. This averaging over a larger area leads to the effect that not only intensity values in the range 22–44 can occur but also other values. For this purpose, a lookup

table with this range as been created according to Eq. (6). Since in our study, the input region consists of an intensity image η and the output region is supposed to be only one average intensity value ρ , we can insert Eq. (13) in (14) to obtain Eq. (15) as follows:

$$\bar{\rho}_t = \frac{1}{N} \sum_{i=-L}^L \sum_{j=-L}^L \eta(\vec{\zeta}(x_a) + i, \vec{\zeta}(y_a) + j). \quad (15)$$

The forecast can then be issued by applying:

$$\widehat{GHI}_{t+\Delta t} = GHI_{CS,t+\Delta t} \cdot k_t(\bar{\rho}_t). \quad (16)$$

Based on the results obtained above (see Table 2), Model 2 is used as the satellite-to-irradiance model translating the obtained intensity η from Eq. (15) to $k_t(\bar{\rho}_t)$.

4.5. Persistence forecast

As a baseline forecast and an alternative when the streamline based forecast cannot be issued (e.g. due to corrupt satellite images), the persistence forecast is defined as:

$$\widehat{GHI}_{kt,t+\Delta t} = GHI_{CS,t+\Delta t} \cdot k_{t,t}, \quad (17)$$

where $GHI_{CS,t}$ refers to the GHI under clear conditions at the time of the forecast and k_t is the calculated clear-sky index with the latest available values. This forecast will be called k_t -persistence in this study. This model is also used as a forecasting reference to evaluate the forecasting skill as discussed in Section 5.3.

4.6. Decision heuristics

An essential step for the operational applicability of a forecasting model is the pre-classification of days to allow an automatized switch into different cloud cover modes. The heuristics to guarantee that the applied method is applicable for the existing and upcoming atmospheric conditions are implemented as follows:

4.6.1. Cloudless domain

In case that the domain of interest is free of clouds, it can be assumed that the clearness persists until clouds start to form or advect into the domain. The domain is assumed as clear if the number of cloudy pixels in the area is lower than 5%. In this case, the model switches to k_t -persistence. This threshold has been chosen empirically to allow for noise in the cloud identification process. The size of the input satellite image is a window of 200 by 200 pixels. Therefore, if $\sum_x \sum_y \beta < 2000$, the issued forecast is solely based on the clear sky model and the latest ground k_t value (k_t -persistence).

4.6.2. Negligible cloud movement speed

If the cloud movement is below 3 pixels per frame ($|\vec{V}| < 3px/frame$), the forecast algorithm also switches to k_t -persistence by extrapolating the latest available k_t value to the forecast horizon of interest. This assumption can

be made since it is very unlikely that clouds will be propelled in or out of the region of interest. These two assumptions have been found highly reliable in the implementation of operational forecasts.

4.7. Short streamline

It can occur that a calculated streamline $\vec{\zeta}$ is shorter than the shift parameter (a) depending on the CMV field. In that case, the last available value of the streamline vector $\vec{\zeta}$ is taken as the identified pixel. This is only an approximation, nevertheless it is useful to continuously issue a forecast.

4.8. Data quality control

Occasionally, satellite images were not online, not downloaded correctly or the downloaded image was corrupt. Additionally, the stream of ground measurements could be interrupted by instrument malfunction, connectivity issues or maintenance work. If the issues with the input data could be detected, the forecasting system automatically switches to the k_t -persistence model. In this way, a forecast is continuously issued while the achieved skill for those days is zero. Approximately 10% of all days used for this study contained corrupt data of some sort and therefore have been excluded from the evaluation of the forecasting capabilities.

5. Model evaluations

To evaluate the performance of the proposed satellite-to-irradiance and forecasting model, they have been implemented for San Diego, California (longitude: 32.88; latitude: -117.23). The satellite-to-irradiance model has been evaluated for 100 days covering a time period from 20-March-2013 to 27-June-2013. The development of the forecasting method, including the implementation of the mentioned heuristics, has been done on a data set covering images and ground measurements from 13-October-2013 09:00 Pacific Daylight Time until 15-January-2014 15:45:00 for a total of 80 days in that period. This set is referred to as the development set. The method derived and implemented with the development set was then applied to a validation set covering the time period from 21-March-2013 09:00 until 07-July-2013 15:45 containing 110 days of data. The results obtained with both data sets for 1h-, 2h- and 3h-ahead forecast horizons are discussed and analyzed in this section. A quantitative and qualitative error analysis, including a comparison to the results of previously proposed methods, covering the same forecast horizons are presented. The evaluation of the model is based on the metrics defined below.

5.1. Evaluation metrics

Current research efforts in the solar forecasting field have led to numerous approaches to evaluate the applica-

bility and compare different forecasting methods. To provide an accurate representation of the capabilities of the forecasting methods proposed in this study, several metrics are used. For a more detailed description about common ways to describe the performance of solar forecasts, refer to [Marquez and Coimbra \(2013b\)](#). The error metrics mean bias error (*MBE*), mean absolute error (*MAE*), root mean square error (*RMSE*) and the cross-correlation (*xcor*) are used here:

$$MBE = \frac{1}{N} \sum_{i=1}^N (GHI_{GT,i} - \widehat{GHI}_i), \quad (18)$$

$$MAE = \frac{1}{N} \sum_{i=1}^N |GHI_{GT,i} - \widehat{GHI}_i|, \quad (19)$$

$$RMSE = \sqrt{\frac{1}{N} \sum_{i=1}^N (GHI_{GT,i} - \widehat{GHI}_i)^2}, \quad (20)$$

$$xcor = \frac{\sum_{i=1}^N ((GHI_{GT,i} - \overline{GHI}_{GT}) \cdot (\widehat{GHI}_i - \overline{\widehat{GHI}}))}{\sqrt{\sum_{i=1}^N (GHI_{GT,i} - \overline{GHI}_{GT})^2 \cdot \sum_{i=1}^N (\widehat{GHI}_i - \overline{\widehat{GHI}})^2}}, \quad (21)$$

these statistics are calculated and presented in [Tables 2 and 3](#). Additionally to the values calculated in $W m^{-2}$, it is possible to calculate relative values of the forecast performance with the average ground truth value as a reference (\overline{GHI}_{GT}). These relative values of the error are indicated with a prefixed *r*. To provide an important evaluation criteria to measure the forecast quality and to make results comparable to other forecast approaches (e.g. [Marquez and Coimbra, 2013b](#); [Chu et al., 2013](#); [Quesada-Ruiz et al., 2014](#)), the forecasting skill is calculated as:

$$s = 1 - \frac{RMSE_{\widehat{GHI}}}{RMSE_{k_t-pers.}}. \quad (22)$$

For a perfect forecast $s = 1$ would be obtained, while a negative forecasting skill occurs as soon as $RMSE_{\widehat{GHI}} > RMSE_{k_t-pers.}$. A negative forecasting skill indicates that the assumptions of the upcoming sky conditions are erroneous.

To describe the probability of occurrence of forecasting errors of different magnitudes, the cumulative distribution function (*CDF*) is used. The *CDF* of forecasting error magnitudes is given by:

$$CDF_{Err.}(X) = P(Err. \leq X), \quad (23)$$

where $P(Err. \leq X)$ represents the probability that the error $Err. = GHI_{GT} - \widehat{GHI}$ lies below a certain *X*. The probability density function has been calculated for 75 probability increments (bins).

5.2. Satellite-to-irradiance model results

Results of Model 1 and Model 2 compared to ground measurements are shown in [Table 2](#), [Figs. 4 and 5](#). It can be seen that Model 2 outperforms Model 1. [Fig. 4](#) shows the modeled data versus ground measurements for six consecutive days as an example for San Diego. While both models perform equally on clear days, the lookup table based model performs significantly better on overcast days. [Table 2](#) shows the capabilities of the two satellite-to-irradiance models for the pre-processed satellite images, compared to the results from the SUNY model. Due to availability, the SUNY data covers the same days but for the previous year. After the exclusion of suspected outliers, the SUNY model shows similar characteristics to the results of our model. As mentioned above, the SUNY model has been intensively validated with ground measurements (e.g. [Nottrott and Kleissl, 2010](#); [Gueymard and Wilcox, 2011](#); [Djebbar et al., 2012](#); [Vignola et al., 2007](#); [Nonnenmacher et al., 2014](#)). These studies found that the SUNY model is in good agreement with ground

Table 3

Results of the proposed deterministic forecasting model, for forecast horizons of 1h-, 2h- and 3h-ahead. The same table shows the statistics obtained with k_t -persistence as well as the forecast skill.

	Data set size	Mean forecast ($W m^{-2}$)	Mean measured ($W m^{-2}$)	<i>MBE</i> ($W m^{-2}$)	<i>rMBE</i> (%)	<i>MAE</i> ($W m^{-2}$)	<i>rMAE</i> (%)	<i>RMSE</i> ($W m^{-2}$)	<i>rRMSE</i> (%)	<i>xcor</i> (–)	Skill (–)
<i>Development set</i>											
60 min Sat	1371	442.21	442.32	–0.12	–0.03	39.04	8.83	78.98	17.86	0.90	r9.01
k_t -persistence	1371	436.06	442.32	–6.26	–1.44	42.06	9.64	86.80	19.91	0.88	
120 min Sat	1180	427.53	441.25	–13.72	–3.21	45.10	10.55	86.14	20.15	0.89	r11.64
k_t -persistence	1180	427.53	417.82	9.71	2.27	50.55	11.82	97.49	22.80	0.86	
180 min Sat	1019	285.43	275.94	9.49	3.32	38.90	13.63	71.34	24.99	0.93	r18.74
k_t -persistence	1019	267.47	275.94	–8.47	–3.17	46.95	17.55	87.73	32.80	0.89	
<i>Validation set</i>											
60 min Sat	2026	773.73	759.43	14.29	1.85	66.66	8.62	129.68	16.76	0.83	r8.10
k_t -persistence	2026	745.69	759.43	–13.74	–1.84	73.99	9.92	141.11	18.92	0.81	
120 min Sat	1680	762.61	753.33	9.28	1.22	75.35	9.88	144.98	19.01	0.79	r11.32
k_t -persistence	1680	730.99	753.33	–22.35	–3.06	88.60	12.12	163.48	22.36	0.74	
180 min Sat	1336	601.03	585.38	15.65	2.60	83.43	13.88	139.92	23.28	0.83	r15.77
k_t -persistence	1336	568.04	585.38	–17.34	–3.05	99.03	17.43	166.11	29.24	0.76	

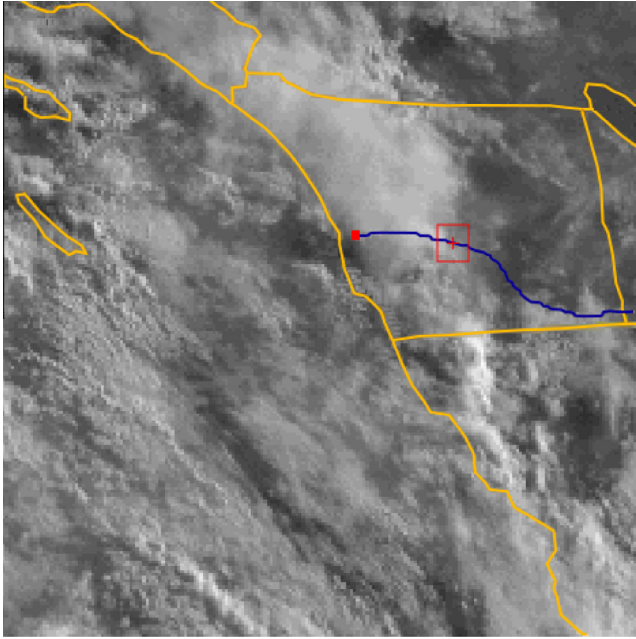


Fig. 3. Example of a quality enhanced $Im_{t=2}$ frame with a superimposed streamline, calculated based on the flow velocity field. The solid line indicates the streamline while the small square shows San Diego (end of streamline). The dashed boxed area represents the region of interest that is likely to be propelled to San Diego within the next forecasting time step (here: 1h).

measurements for the majority of covered regions (problems only exist in regions with snow cover and extensive overcast periods). This allows the assumption that both satellite-to-irradiance model approaches shown above are valid for all locations covered by *NOAA* images if no snow cover is present. Therefore, this approach can be considered as a valuable tool for researchers to model GHI at any given location in North America near real time, while Model 2 outperforms Model 1. Fig. 5 shows a scatter plot

of GHI_{GT} versus GHI_{M1} as well as GHI_{GT} versus GHI_{M2} . Points where GHI_{M1} and GHI_{M2} coincide are highlighted. These values are equal since there are no clouds detected in the satellite image ($\rho = 0$). Errors of larger magnitude appear almost exclusively on the upper half of the 1:1 line. We can assume that those errors are due to the image processing or cloud segmentation rather than in the satellite-to-irradiance model. During those times of large error magnitude, the satellite images appear to be clear while the GHI_{GT} signal is clearly attenuated by clouds.

5.3. Forecasting model results

The results of the described deterministic GHI prediction model are summarized in Table 3 and visualized in Figs. 6 and 7. The skill achieved for continuous operation of this method is between 8% and 19% over the persistence model. The forecasting skill increases with the forecast horizon, mostly because the sky conditions are more likely to change over longer time horizons. Therefore, the usability of the k_t -persistence model decreases with increasing time horizon leading to a better relative performance of the forecast model. This also becomes clear by comparing the increasing surface between the CDF curves in Fig. 7 with increasing time horizon. The figure additionally shows that the achieved skill over persistence is only generated by reducing the occurrence of positive errors, while the proposed model is slightly worse than k_t -persistence for negative errors. The skill achieved with the proposed method is on the same order of magnitude as of previously proposed satellite based methods (Marquez et al., 2013; Hammer et al., 2003). However, the reported skill achieved with satellite images, ground telemetry and artificial neural networks (ANNs) are higher, between 18% and 25% (Marquez et al., 2013). These methods rely heavily on ground measurements and extensive ANN training. The error for the

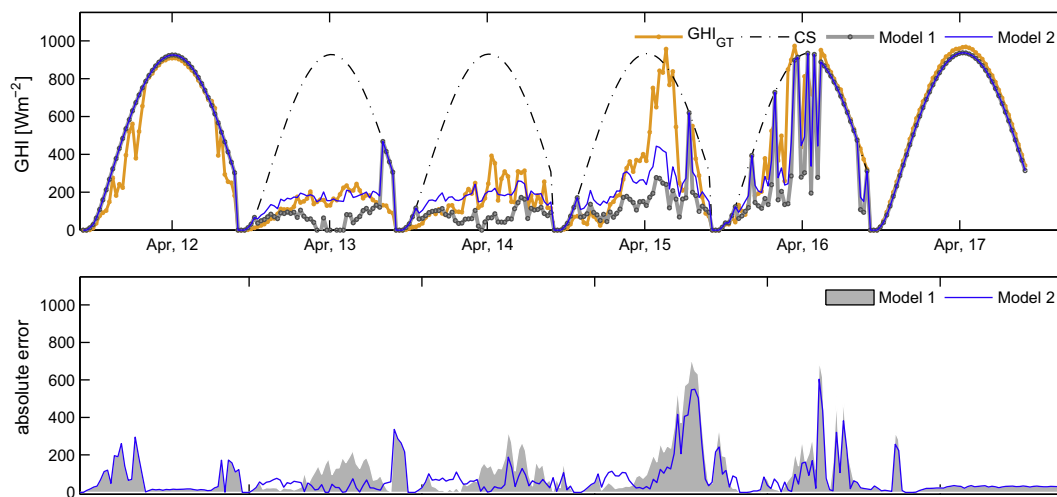


Fig. 4. Comparison of six days in April 2013 of ground measured GHI_{GT} values (MFR-7) and values derived from the satellite-to-irradiance models described above (Model 1 and Model 2). Both satellite-to-irradiance models perform the same on clear days while the lookup table approach (Model 2) achieves better results on overcast days. CS indicates modeled GHI values under clear sky conditions.

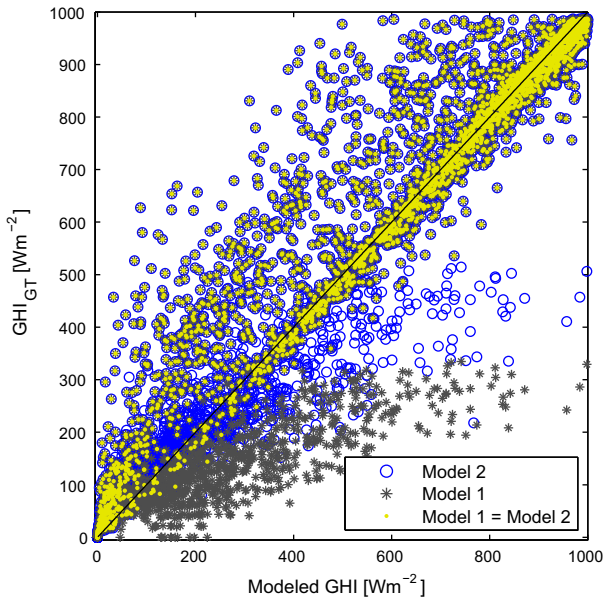


Fig. 5. Scatter plot of GHI_{GT} against the values obtained with GHI_{M1} and GHI_{M2} . It can be seen that the error of Model 2 is generally smaller than from Model 1. Model 1 tends to underestimate irradiance under overcast conditions. This is due to the fact that for Model 2 $k_{t,min} = 0.16$ while Model 1 allows for $k_{t,min} = 0$ which cannot occur during daylight times. Yellow markers indicate that values from Model 1 equal values of Model 2, obtained when $\rho = 0$ in the satellite image. In these cases, the resulting errors are large and due to undetected clouds in the satellite image. (For interpretation of the references to colour in this figure legend, the reader is referred to the web version of this article.)

1h-ahead ($rMAE = 8.83\%$ and 8.62%) forecast is of lower magnitude than other solely deterministic models (e.g. Hammer et al., 1999 $rMAE = 12\text{--}15\%$). A comparison of our results to the results mentioned by Perez et al. (2010) suggests that our new method can be used in addition or

as an alternative and provide similar or better results, depending on the location specific irradiance characteristics. Additionally, the temporal resolution of this forecast with an update every 15 min is higher than for the cited studies (Hammer et al., 1999, 2003; Marquez et al., 2013). Fig. 6 provides an example of the results of the proposed forecasting model compared to ground truth values and the k_t -persistence model. This sequence of consecutive days has been chosen as an example because it covers various sky conditions. In general, the forecasting method reduces the error compared to k_t -persistence. This characteristic is consistent with the positive forecasting skill for all forecast horizons (see Table 3). Since there are multiple layers of data processing in this study, a closer look at the critical sources of error helps to clarify the origin of overall errors. The forecasting performance (and thus the skill) of the proposed method is limited by the accuracy of the satellite-to-irradiance model. Additional sources of error are due to image processing, inaccurate cloud tracking and the simplifications made with the frozen cloud assumption. An example of a typical error is shown in Fig. 6 where a non-captured ramp event in the GHI_{GT} signal occurs mid-day on 16-October-2013. For this particular event, the cloud image appears to be clear while a significant GHI attenuation is measured on the ground. This type of error is caused normally during to the image transfer and preliminary processing of the satellite images.

6. Conclusions

A remote sensing-based GHI forecasting methodology was proposed and successfully applied to predict 15 min averages of GHI on the Earth surface for 1h-, 2h- and 3h

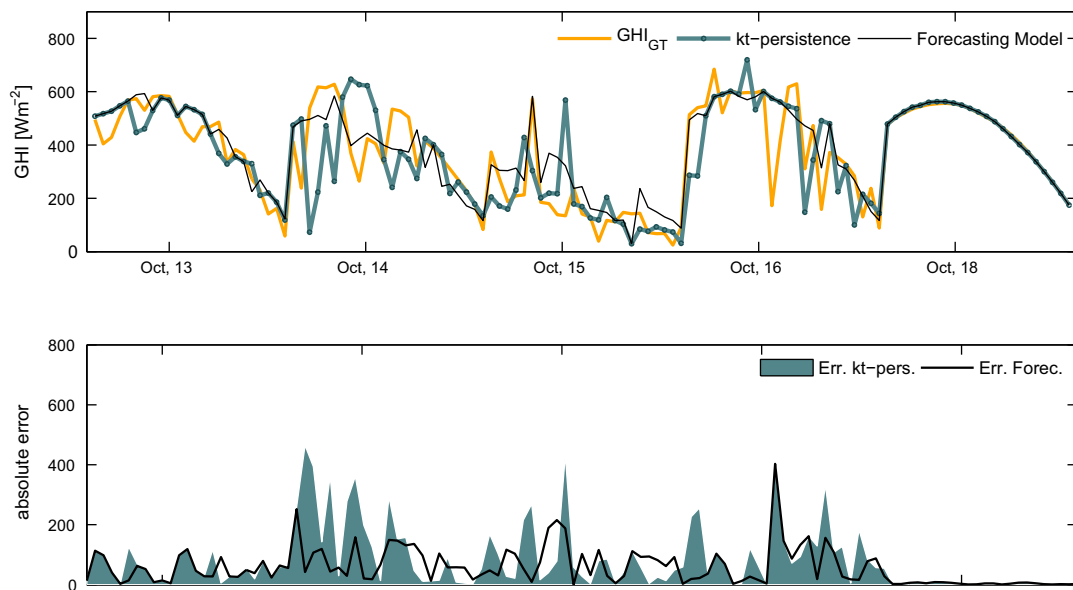


Fig. 6. Comparison of five example days in October 2013 of ground measured GHI_{GT} values, results from the proposed 1h-ahead forecasting method and results from the k_t -persistence model. The second part of the figure shows the error of both models. The proposed forecasting model reduces the error between ground truth and the forecasted values compared to the error of k_t -persistence.

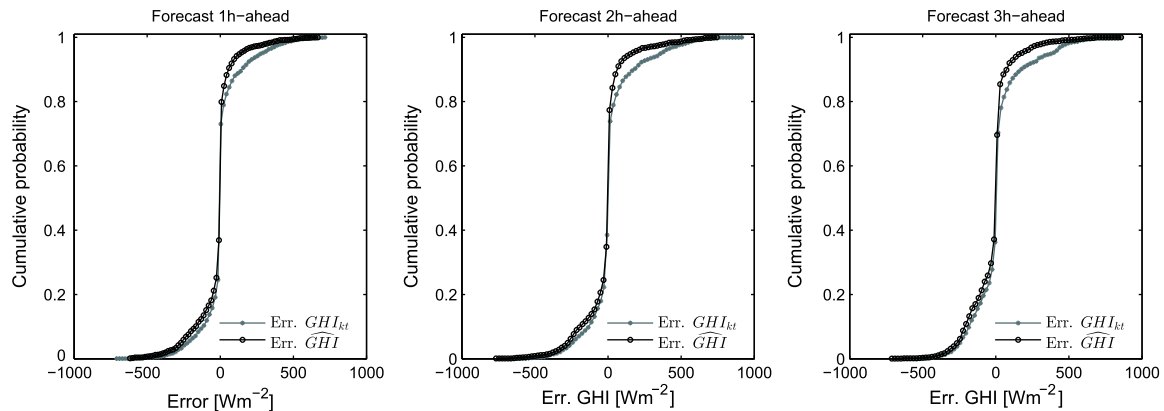


Fig. 7. Cumulative distribution function for the errors obtained with the validation set for forecast horizons 1h, 2h and 3h ahead, respectively. The overall performance increases with the time horizon (the surface between the curves increases). This is consistent with the increasing forecasting skill for longer forecasting horizons. In general, the errors occurring with the forecasting model are smaller than for the k_t -persistence model. However, the major improvement of the forecasting model over the k_t -persistence model is for positive errors of small to medium magnitudes (0–500 W m^{-2}).

ahead. This forecast is based uniquely on satellite images and ground measurements with no other inputs. The overall methodology includes the following main steps: (1) Application of a fast cloud segmentation method on pre-processed satellite images. The method works reliably for optically thick clouds that are easily distinguishable from the background while problems with optically thin (opaque) clouds remain. Since the attenuation of GHI by optically thin clouds is limited, this caveat of the method introduces only limited errors to the forecasts. (2) Calculation of cloud movement vectors between two satellite frames with the optical flow algorithm. The optical flow approach is found to be superior to *PIV* and *DCA*. A direct evaluation of the cloud tracking method is not possible due to the lack of ground truth data for cloud velocities. However, the fact that a positive forecasting skill is achieved encourages the assumption that cloud tracking based on optical flow yields significant values for cloud transport. (3) Based on this cloud movement vector field, the streamline passing through the region of interest and the average speed is calculated. Therefore, a region of pixels that are most likely to move to the region of interest can be identified. (4) A satellite-to-irradiance model translates the intensity values of these pixels into the GHI forecast. Since this method relies on the accuracy of the satellite-to-irradiance model, a novel, fast processing approach to enhance the satellite-to-irradiance model with ground truth is proposed. The novelty of this approach lies in the utilization of online near-real time available pre-processed images combined with the fast assignment of clear sky index values from a lookup table. The provided lookup table can be used for all locations covered by the satellite images. If ground measurements area available for a specific location, the lookup table can easily be created to enhance accuracy. The proposed satellite-to-irradiance model outperforms the linear approach by reducing the $RMSE$ from 124.53 W m^{-2} to 107.41 W m^{-2} .

While substantial heuristics have been used to achieve the highest possible forecasting skill on the development

set, the implementation has been applied to an independent test set. This approach yields a forecasting skill ranging from 8% to 19% over persistence for San Diego for forecast horizons between 1-h of up to 3-h. Previously reported forecasting skills for the same forecast horizons are on the same order of magnitude between 5% and 25%, however they are not directly comparable to the results presented here due to different test locations. San Diego is a notoriously difficult region to forecast due to frequent inversion layers in the Southern California coast. While other methods yield comparable forecasting skills, the intra-day forecasting system proposed here is especially valuable due to the low computation costs and because it is solely based on satellite images and ground measurements. Our calculations also show that there is room for further optimization of this method, particularly in relation to the detection of optically thin clouds.

Acknowledgments

The authors gratefully acknowledge the partial financial support given by the California Public Utilities Commission (CPUC) under the California Solar Initiative (CSI) Program, and the partial support by the National Science Foundation (NSF) EECS (EPAS) Award No. 1201986, which is managed by Dr. Paul Werbos.

References

- Beyer, H.G., Costanzo, C., Heinemann, D., 1996. Modifications of the Heliosat procedure for irradiance estimates from satellite images. *Sol. Energy* 56 (3), 207–212.
- Black, M.J., Anandan, P., 1996. The robust estimation of multiple motions: parametric and piecewise-smooth flow fields. *Comput. Vis. Image Understand.* 63 (1), 75–104.
- Bruhn, A., Weickert, J., Schnörr, C., 2005. Lucas/Kanade meets Horn/Schunck: combining local and global optic flow methods. *Int. J. Comput. Vis.* 61, 211–231.
- Cano, D., Monget, J.M., Albuissou, M., Guillard, H., Regas, N., Wald, L., 1986. A method for the determination of the global solar radiation from meteorological satellite data. *Sol. Energy* 37 (1), 31–39.

- Chow, C.W., Urquhart, B., Lave, M., Dominguez, A., Kleissl, J., Shields, J., Washom, B., 2011. Intra-hour forecasting with a total sky imager at the UC San Diego solar energy testbed. *Sol. Energy* 85 (11), 2881–2893.
- Chu, Y., Pedro, H.T.C., Coimbra, C.F.M., 2013. Hybrid intra-hour DNI forecasts with sky image processing enhanced by stochastic learning. *Sol. Energy* 98 (Part C), 592–603.
- Collet, C., Quinquis, A., Boucher, J.M., 1992. Cloudy sky velocity estimation based on optical flow estimation leading with an entropy criterion. In: *Proceedings, 11th IAPR International Conference on Pattern Recognition*, 1992. Conference C: Image, Speech and Signal Analysis, vol. III, pp. 160–163.
- Djebbar, R., Morris, R., Thevenard, D., Perez, R., Schlemmer, J., 2012. Assessment of SUNY version 3 global horizontal and direct normal solar irradiance in Canada. *Energy Procedia* 30 (0), 1274–1283.
- Dong, Z., Yang, D., Reindl, T., Walsh, W.M., 2013. Short-term solar irradiance forecasting using exponential smoothing state space model. *Energy* 55 (0), 1104–1113.
- Endlich, R.M., Wolf, D.E., 1981. Automatic cloud tracking applied to GOES and METEOSAT observations. *J. Appl. Meteorol.* 20 (3), 309–319.
- Escrig, H., Batlles, F.J., Alonso, J., Baena, F.M., Bosch, J.L., Salbidegoitia, I.B., Burgaleta, J.I., 2013. Cloud detection, classification and motion estimation using geostationary satellite imagery for cloud cover forecast. *Energy* 55 (0), 853–859.
- Ghonima, M.S., Urquhart, B., Chow, C.W., Shields, J.E., Cazorla, A., Kleissl, J., 2012. A method for cloud detection and opacity classification based on ground based sky imagery. *Atmos. Meas. Tech.* 5 (11), 2881–2892.
- Girodo, M., Mueller, R.W., Heinemann, D., 2006. Influence of three-dimensional cloud effects on satellite derived solar irradiance estimation – first approaches to improve the Heliosat method. *Sol. Energy* 80 (9), 1145–1159.
- Gueymard, C.A., 2012. Clear-sky irradiance predictions for solar resource mapping and large-scale applications: improved validation methodology and detailed performance analysis of 18 broadband radiative models. *Sol. Energy* 86 (8), 2145–2169.
- Gueymard, C.A., Wilcox, S.M., 2011. Assessment of spatial and temporal variability in the US solar resource from radiometric measurements and predictions from models using ground-based or satellite data. *Sol. Energy* 85 (5), 1068–1084.
- Guillot, E.M., Haar, T.H.V., Forsythe, J., Fletcher, S., 2012. Evaluating satellite-based cloud persistence and displacement nowcasting techniques over complex terrain. *Weather Forecasting* 27, 502–514.
- Hammer, A., Heinemann, D., Hoyer, C., Kuhlemann, R., Lorenz, E., Müller, R., Beyer, H.G., 2003. Solar energy assessment using remote sensing technologies. *Rem. Sens. Environ.* 86 (3), 423–432.
- Hammer, A., Heinemann, D., Lorenz, E., Lucke, B., 1999. Short-term forecasting of solar radiation: a statistical approach using satellite data. *Sol. Energy* 67, 139–150.
- Handa, Y., Kurtz, B., Nguyen, D., Urquhart, B., Chow, C.W., Ghonima, M., Kleissl, J., 2014. Solar irradiance forecasting using a ground-based sky imager developed at UC san diego. *Sol. Energy* 103 (0), 502–524.
- Horn, B.K., Schunck, B.G., 1981. Determining optical flow. *Artif. Intell.* 17 (1), 185–203.
- Ineichen, P., 2006. Comparison of eight clear sky broadband models against 16 independent data banks. *Sol. Energy* 80 (4), 468–478.
- Ineichen, P., Perez, R., 2002. A new air mass independent formulation for the Linke turbidity coefficient. *Sol. Energy* 73 (3), 151–157.
- Inman, R.H., Pedro, H.T.C., Coimbra, C.F.M., 2013. Solar forecasting methods for renewable energy integration. *Prog. Energy Combust. Sci.* 39 (6), 535–576.
- Leung, I.J.H., Jordan, J.E., 1995. Image processing for weather satellite cloud segmentation. In: *Canadian Conference on Electrical and Computer Engineering*, 1995, vol. 2. IEEE, pp. 953–956.
- Lorenz, E., Heinemann, D., Wickramaratne, H., Beyer, H.G., Bofinger, S., 2007. Forecast of ensemble power production by grid-connected PV systems. In: *Proceedings of the 20th European PV Conference*, Milano, Italy.
- Marquez, R., Coimbra, C.F.M., 2013a. Intra-hour DNI forecasting methodology based on cloud tracking image analysis. *Sol. Energy* 91 (0), 327–336.
- Marquez, R., Coimbra, C.F.M., 2013b. Proposed metric for evaluation of solar forecasting models. *ASME J. Sol. Energy Eng.* 135 (1), 0110161–0110169.
- Marquez, R., Pedro, H.T.C., Coimbra, C.F.M., 2013. Hybrid solar forecasting method uses satellite imaging and ground telemetry as inputs to ANNs. *Sol. Energy* 92, 176–188.
- Martins, F.R., Pereira, E.B., Abreu, S.L., 2007. Satellite-derived solar resource maps for Brazil under SWERA project. *Sol. Energy* 81 (4), 517–528.
- Mathiesen, P., Kleissl, J., 2011. Evaluation of numerical weather prediction for intra-day solar forecasting in the continental united states. *Sol. Energy* 85 (5), 967–977.
- Mueller, R.W., Dagestad, K.F., Ineichen, P., Schroedter-Homscheidt, M., Cros, S., Dumortier, D., Kuhlemann, R., Olseth, J.A., Piernavieja, G., Reise, C., Wald, L., Heinemann, D., 2004. Rethinking satellite-based solar irradiance modeling: the SOLIS clear-sky module. *Rem. Sens. Environ.* 91 (2), 160–174.
- Mueller, R.W., Matsoukas, C., Gratzki, A., Behr, H.D., Hollmann, R., 2009. The CM-SAF operational scheme for the satellite based retrieval of solar surface irradiance a LUT based eigenvector hybrid approach. *Rem. Sens. Environ.* 113 (5), 1012–1024.
- Nakariyakul, S., 2013. Fast spatial averaging: an efficient algorithm for 2D mean filtering. *J. Supercomput.* 65 (1), 262–273.
- Nonnenmacher, L., Kaur, A., Coimbra, C.F.M., 2014. Verification of the SUNY direct normal irradiance model with ground measurements. *Sol. Energy* 99 (0), 246–258.
- Nottrott, A., Kleissl, J., 2010. Validation of the NSRDB–SUNY global horizontal irradiance in California. *Sol. Energy* 84 (10), 1816–1827.
- Pereira, E.B., Martins, F.R., Abreu, S.L., Couto, P., Stuhlmann, R., Colle, S., 2000. Effects of burning of biomass on satellite estimations of solar irradiation in Brazil. *Sol. Energy* 68 (1), 91–107.
- Perez, R., Ineichen, P., Moore, K., Kmiecik, M., Chain, C., George, R., Vignola, F., 2002. A new operational model for satellite-derived irradiances: description and validation. *Sol. Energy* 73 (5), 307–317.
- Perez, R., Kivalov, S., Schlemmer, J., Hemker, K., Renne, D., Hoff, T.E., 2010. Validation of short and medium term operational solar radiation forecasts in the US. *Sol. Energy* 84 (5), 2161–2172.
- Quesada-Ruiz, S., Chu, Y., Tovar-Pescador, J., Pedro, H.T.C., Coimbra, C.F.M., 2014. Cloud-tracking methodology for intra-hour DNI forecasting. *Sol. Energy* 102 (0), 267–275.
- Schillings, C., Mannstein, H., Meyer, R., 2004. Operational method for deriving high resolution direct normal irradiance from satellite data. *Sol. Energy* 76 (4), 475–484.
- Shi, H., 1998. Cloud movement detection for satellite images. In: *1998 Fourth International Conference on Signal Processing Proceedings*, 1998. ICSP '98, vol. 2, pp. 982–985.
- Sun, D., Roth, S., Black, M.J., 2010. Secrets of optical flow estimation and their principles. In: *2010 IEEE Conference on Computer Vision and Pattern Recognition (CVPR)*, 2010. IEEE, pp. 2432–2439.
- Sun, D., Roth, S., Black, M.J., 2014. A quantitative analysis of current practices in optical flow estimation and the principles behind them. *Int. J. Comput. Vis.* 106 (2), 115–137.
- Vignola, F., Harlan, P., Perez, R., Kmiecik, M., 2007. Analysis of satellite derived beam and global solar radiation data. *Sol. Energy* 81 (6), 768–772.
- Wu, Q.X., 1995. A correlation-relaxation-labeling framework for computing optical flow-template matching from a new perspective. *IEEE Trans. Pattern Anal. Mach. Intell.* 17 (9), 843–853.